

Zinc Immobilization and Magnetite Formation via Ferric Oxide Reduction by *Shewanella putrefaciens* 200

D. CRAIG COOPER,* FLYNN PICARDAL, JASON RIVERA, AND CATHERINE TALBOT
School of Public and Environmental Affairs,
Indiana University, Bloomington, Indiana 47405

Long-term batch experiments in an artificial groundwater medium indicated that microbial reduction of synthetic, high-surface-area goethite and lepidocrocite by *Shewanella putrefaciens* 200 can act to immobilize surface-associated zinc into a new mineral phase that is not soluble in 0.5 M HCl. While Zn was incorporated in siderite grains in experiments with goethite, additional Zn immobilization may result from incorporation into as yet unidentified biogenic minerals or into a more crystalline goethite. Experiments with an oxide mixture primarily composed of lepidocrocite resulted in the production of magnetite, biphasic immobilization of Zn, and an enhanced overall degree of Zn immobilization. When NO_3^- was present as an alternate electron acceptor, microbial production of Fe(II) was inhibited, and the degree of Zn immobilization was subsequently reduced. These data indicate that (i) biologically induced mineralization can play a key role in the cycling of trace elements in natural systems, (ii) the nature of the oxide surface plays an important role in biologically induced mineralization, and (iii) conditions associated with Fe(II) production are necessary for these processes to immobilize surface-bound Zn within these new mineral phases.

Introduction

Over the past two decades, dissimilatory reduction of ferric iron minerals has been documented for a wide range of microorganisms in a broad range of environments (1–4) and has become recognized as an important constituent of the global carbon and iron cycles (3, 5, 6). Surprisingly little, however, has been published with respect to the effect of this process on the surface chemistry of the iron oxide. Microbial reduction of amorphous ferric oxyhydroxide ($\text{Fe}(\text{OH})_3$) has been reported to induce the formation of magnetite (6–11). Recently, Frederickson et al. (12) reported that, depending upon the composition of the aqueous medium, microbial reduction of hydrous ferric oxide resulted in the production of magnetite (Fe_2O_3), siderite (FeCO_3), vivianite ($\text{Fe}_3(\text{PO}_4)_2$), and/or green rust type compounds ($[\text{Fe}^{II}_{(6-x)}\text{Fe}^{III}_x(\text{OH})_{12}]^{x+}[(\text{A}^{2-})_{x/2}\cdot y\text{H}_2\text{O}]^{x-}$). The composition of the aqueous medium also affected the rate and extent of iron reduction and the degree of crystallinity of the solids produced by biologically induced mineralization. Synthetic green rusts (ferrous/ferric minerals that also occur naturally) have been shown to chemically reduce NO_3^- (13, 14) and

NO_2^- (15, 16), and it is likely that their formation can be induced by microbial iron reduction. If microbial alteration of localized pH and Eh conditions (7, 8) is severe enough to induce new diagenetic pathways for iron and NO_x^- anions, then one would expect these same processes to play an important role in the cycling of the many metals known to interact strongly with iron oxide surfaces (17).

Microbial reduction of an iron oxy-hydroxide mineral ultimately results in the reductive dissolution of that mineral in the immediate region of the microbe. This dissolution releases Fe(II) and OH^- into solution and has been reported to release surface-bound metals and metalloids into solution as well (3, 18). After the initial release, the metal (and Fe(II)) can adsorb back onto the oxide surface, adsorb onto the microbial cell surface, precipitate as a new mineral phase, or remain as an aqueous ion or complex. The cell walls of both Gram-negative and Gram-positive bacteria strongly adsorb metals (19–22), and microbial cell surfaces act as nucleation sites for the precipitation of new mineral phases that incorporate metals adsorbed to the microbial surface into their crystal structure (23–26). In addition, release of OH^- during iron oxyhydroxide mineral reduction is believed to create localized regions of elevated pH. Such pH modifications will lead to a greater degree of cation adsorption and may lead to the precipitation of mineral assemblages that are not predicted from bulk solution composition. Thus, dissimilatory iron reduction can play an important role in cycling and speciation of metals in anoxic sediments and groundwater.

Shewanella putrefaciens is a facultative anaerobe capable of utilizing O_2 , NO_3^- , NO_2^- , Fe(III), Mn(IV), and a number of other compounds as terminal electron acceptors for carbon metabolism (3). This microorganism has been found in a number of freshwater and marine environments and has been the subject of research that has examined its ability to reduce a variety of respiratory substrates (27–30) and anaerobically transform carbon tetrachloride (31, 32). Zinc is a common pollutant metal and one of the most common metallic contaminants found in the groundwater and sediments underlying Department of Energy facilities (33). Zinc possesses only two oxidation states (Zn^0 , Zn^{2+}), has a goethite adsorption edge at approximately pH 6.8 (34), and interacts relatively weakly with most inorganic ligands. These qualities make zinc an excellent candidate for initial investigations into the effect of microbial iron reduction on metal speciation in anoxic groundwater systems. It is, therefore, the objective of this study to determine the nature of the changes in chemical speciation of a model metal (Zn) as the result of microbial reduction of goethite and lepidocrocite by *S. putrefaciens* in an artificial groundwater slurry. Since NO_3^- is sometimes a cocontaminant at certain sites and has been shown to affect rates of microbial iron reduction (27, 29, 35), we also examined the effect of NO_3^- on Zn speciation during microbial reduction of iron minerals.

Materials and Methods

Microorganism and Culture Conditions. *S. putrefaciens* is a Gram negative, motile rod with an obligate respiratory metabolism (36). The strain used in these experiments, *S. putrefaciens* 200, was originally isolated from a Canadian oil pipeline by Obuekwe (37). The culture was maintained on solid medium of nutrient agar containing 5 g L^{-1} of yeast extract (Difco, Detroit, MI) as previously described (31). Liquid cultures were grown in a 2.5-L Bioflow 3000 Fermentor (New Brunswick Scientific Company, Edison, NJ) in a medium that consisted (per liter) of 2.0 g of Na_2SO_4 , 0.5 g of K_2HPO_4 , 1.0

* Corresponding author phone: (812)855-0730; fax: (812)855-7802; e-mail: dacooper@indiana.edu.

g of NH_4Cl , 0.198 g of $\text{CaCl}_2 \cdot 2\text{H}_2\text{O}$, 0.1 g of $\text{MgSO}_4 \cdot 7\text{H}_2\text{O}$, 19.35 mg of $\text{FeCl}_3 \cdot 6\text{H}_2\text{O}$, 0.5 g of yeast extract, and 3 mL of 60% (w/v) sodium lactate. Following an initial period of aerobic growth, anaerobic reductase activity was induced by reducing the air-flow to approximately 100 mL min^{-1} and maintaining the cells under microaerobic ($[\text{O}_2]_{(\text{aq})} < 2.5 \mu\text{mol L}^{-1}$) conditions for a period of 12 h. *S. putrefaciens* cells were harvested by centrifugation and resuspended to a target optical density ($A_{600} = \sim 1.2$) in artificial groundwater (AGW) medium.

Preparation of Iron Oxide Slurries. Fresh anaerobic AGW medium was used for every experiment. The major ion composition of the AGW medium was $560 \mu\text{mol L}^{-1} \text{ Ca}^{2+}$, $1053 \mu\text{mol L}^{-1} \text{ Cl}^-$, $500 \mu\text{mol L}^{-1} \text{ HCO}_3^-$, $245 \mu\text{mol L}^{-1} \text{ of K}^+$, $243 \mu\text{mol L}^{-1} \text{ of Mg}^{2+}$, $438 \mu\text{mol L}^{-1} \text{ of NH}_4^+$, $44 \mu\text{mol L}^{-1} \text{ of PO}_4^{3-}$, and $388 \mu\text{mol L}^{-1} \text{ of SO}_4^{2-}$. The minor constituents of this medium were $190 \mu\text{g L}^{-1} \text{ of CoCl}_2 \cdot 6\text{H}_2\text{O}$, $2 \mu\text{g L}^{-1} \text{ of CuCl}_2 \cdot 2\text{H}_2\text{O}$, $6 \mu\text{g L}^{-1} \text{ of H}_3\text{BO}_3$, $100 \mu\text{g L}^{-1} \text{ of MnCl}_2 \cdot 6\text{H}_2\text{O}$, $36 \mu\text{g L}^{-1} \text{ of Na}_2\text{MoO}_4$, $24 \mu\text{g L}^{-1} \text{ of NiCl}_2 \cdot 6\text{H}_2\text{O}$, $144 \mu\text{g L}^{-1} \text{ of ZnSO}_4 \cdot 7\text{H}_2\text{O}$, $2 \mu\text{g L}^{-1} \text{ of biotin}$, $5 \mu\text{g L}^{-1} \text{ of DL Ca pantothenate}$, $2 \mu\text{g L}^{-1} \text{ of folic acid}$, $5 \mu\text{g L}^{-1} \text{ of lipoic acid}$, $5 \mu\text{g L}^{-1} \text{ of nicotinic acid}$, $5 \mu\text{g L}^{-1} \text{ of } p\text{-aminobenzoic acid}$, $10 \mu\text{g L}^{-1} \text{ of pyridoxine HCl}$, $5 \mu\text{g L}^{-1} \text{ of thiamine HCl}$, $5 \mu\text{g L}^{-1} \text{ of riboflavin}$, and $0.1 \mu\text{g L}^{-1} \text{ of vitamin B}_{12}$. In addition, the AGW medium used in these experiments contained $10 \text{ mmol L}^{-1} \text{ of HEPES (Na salt)}$ and $20 \text{ mmol L}^{-1} \text{ of lactate (Na salt)}$. Goethite and lepidocrocite were prepared by oxidation of a ferrous sulfate solution under controlled conditions as documented by Schwertmann and Cornell (38). Goethite and lepidocrocite prepared in this fashion were washed three times with Milli-Q water ($R = 18 \Omega$), freeze-dried, ground, and sieved to $< 150 \mu\text{m}$ (Tyler 100-mesh). A small mass of the solid used in each set of experiments was set aside for X-ray diffraction (XRD) and surface area analyses. It should be noted that our method of goethite and lepidocrocite synthesis resulted in a small amount of ferrihydrite in both preparations and a small amount of goethite in the lepidocrocite. To prepare the experimental slurry, 0.5 g of sieved goethite or lepidocrocite was added to acid-washed, glass serum bottles (nominal 160-mL volume) containing 20 mL of water. This slurry was autoclaved and subsequently cooled in an anaerobic chamber (Coy Laboratory Products) containing 95% N_2 and 5% H_2 . While maintaining anaerobic conditions, 100 mL of sterile AGW medium (concentrated enough to account for a 100–125 mL dilution) was added to the bottles. One milliliter each of sterile, deoxygenated Na lactate (2.5 mol L^{-1}), HEPES (1.25 mol L^{-1}), and Zn (37.5 mmol L^{-1} in 0.01 N HCl) stock solution was added to each bottle. In experiments involving NO_3^- , the bottles were further amended with 1.0 mL of sterile, deoxygenated NaNO_3 stock solution (0.625 mol L^{-1} , 0.312 mol L^{-1} , or 0.125 mol L^{-1} depending on desired NO_3^- concentration). The volume was adjusted to 125 mL with an appropriate volume of sterile deoxygenated water, and the solution was allowed to equilibrate for a period of not less than 48 h.

Fe(III) Reduction Experiments and Extraction Protocols.

Prior to inoculation with *S. putrefaciens*, initial samples (t_0) were taken from each bottle for subsequent analysis. Fe(III) reduction experiments were initiated by inoculating slurries with 2 mL of *S. putrefaciens* suspension under anaerobic conditions. After dilution this resulted in an estimated initial culture optical density (A_{600}) of 0.020, which corresponded to approximately 2×10^6 cells mL^{-1} . Inoculated bottles were crimp-sealed with acid-washed butyl rubber stoppers and incubated horizontally on a shaker table at room temperature. The bottle headspace in all cases was 95% N_2 :5% H_2 .

At each periodic sampling point, bottles were transferred to the anaerobic chamber, shaken to resuspend any settled solids, placed on a magnetic stir-plate, and stirred vigorously enough to generate a small vortex. Slurry aliquots were

withdrawn by pipet and then treated with a series of extractions. For total 0.5 M HCl-soluble Fe(II) and Zn, an aliquot of slurry was transferred to a microcentrifuge tube and extracted in 0.5 M HCl for a period of 2 h (39, 40). The solid was separated by centrifugation (25 min, 14 900g), and an aliquot of supernatant was analyzed within 1 h by a colorimetric ferrozine method (described below). Acidified samples of supernatant for Zn analysis were stored in acid-washed polyethylene bottles for subsequent analysis via flame atomic absorption spectrophotometry (AAS). For 6 M HCl-soluble total iron, Fe(II) and Zn, an aliquot of slurry was pipetted into a microcentrifuge tube, and acid was extracted in 6 M HCl until all solid had dissolved (not less than 4 h). A portion of the solution was stored as described previously for subsequent analysis of total Fe and Zn by AAS. Since colorimetric Fe(II) measurements are not possible at very low pH, an aliquot of the 6.0 M HCl extract was treated with 7.5 M NaOH to decrease acidity to 0.5 M prior to analysis for Fe(II) by the ferrozine technique (described below).

Because NO_2^- rapidly oxidizes Fe(II) in acidic solution, Fe(II) analyses in NO_3^- containing samples had to be performed by a sequential extraction technique. Following centrifugation (25 min, 14 900g) of sediment slurry aliquots under anaerobic conditions, the supernatant was sampled for aqueous Fe(II) and Zn (sample manipulations as described above for total 0.5 M HCl-soluble Fe(II) and Zn). The solid pellet was then suspended in 0.5 M HCl, and remaining analyses (termed Fe(II)-bound and Zn-bound) were performed as has been described for total 0.5 M HCl-soluble Fe(II) and Zn. All sample manipulations prior to acidification were performed inside the anaerobic chamber to prevent oxidation of Fe(II).

Zinc concentrations in acidified extracts were determined by flame AAS using an Instrument Laboratory Video 12 flame atomic absorption spectrophotometer. Fe(II) was analyzed by an adaptation of the ferrozine technique (39, 41). Small aliquots ($\geq 10\times$ dilution factor) of aqueous sample were pipetted directly into 4.5 mL of ferrozine reagent (1 g L^{-1} of ferrozine, 12 g L^{-1} of HEPES). The resultant solution was mixed well and allowed to stand approximately 10 min to allow full color development, and the absorbance at 562 nm was measured on a Shimadzu UV-2101PC UV/vis spectrophotometer. Solution pH was measured inside the anaerobic chamber with a Cole Parmer glass electrode calibrated with pH 4 and pH 7 standard NBS buffers. Zn standards for AAS analysis were prepared by diluting aliquots of certified commercial standards in 0.5 M HCl, and Fe(II) standards were diluted from a concentrated stock solution of ferrous sulfate in 0.5 M HCl. Unless otherwise noted, all solutions were prepared in Milli-Q water ($R = 18 \Omega$). All experiments, extractions, and analyses were performed in acid-washed glassware and plasticware, and procedural blanks consisting of Milli-Q water were sampled at every time point to monitor for potential Zn contamination.

Samples for XRD analysis were prepared by filtering (0.45 μm) 10 mL of slurry solution under an anaerobic atmosphere. Filters were dried for 48 h under an anaerobic atmosphere, then scraped onto a glass slide, and mixed with glycerol or cellulose acetate to prevent oxidation of ferrous minerals. XRD diffractograms were generated on a Phillips XRG 3100 with a Cu-line source. Surface area was measured by five-point BET N_2 adsorption in a Micromeritics Gemini 2360 surface area analyzer, after 2 h degassing under N_2 atmosphere at 120 °C in a Micromeritics Flowprep 060.

These experiments utilized extraction in 0.5 M HCl instead of the more robust citrate dithionite extraction (39), as we were primarily interested in changes in the mobility of surface-bound Zn as a result of microbial iron reduction. Slurry aliquots were extracted in both 0.5 and 6 M HCl (rather than citrate dithionite which might introduce an increased

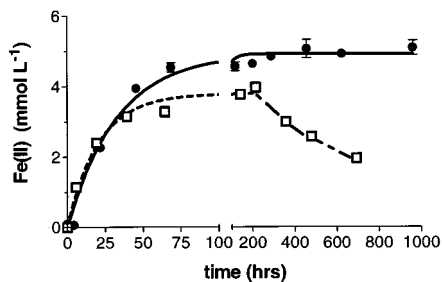


FIGURE 1. Fe(II) production by dissimilatory reduction of synthetic goethite (solid circles) and lepidocrocite (open squares) by *S. putrefaciens* in the absence of NO_3^- . Given concentrations represent the sum of aqueous + bound fractions. Trend lines represent the best nonlinear fit to the data.

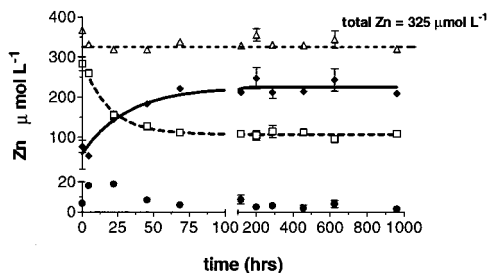


FIGURE 2. Zinc immobilization as a result of microbial goethite reduction in the absence of NO_3^- . Zn-aqueous (solid circles), Zn-bound (open squares), Zn-strongly bound (solid diamonds), and Zn-total (open triangles) are plotted versus time (h). Trend lines represent best nonlinear fit to the data.

degree of Zn contamination) to monitor the mass balance of total Zn within the experimental system.

Results

Results from iron reduction experiments with *S. putrefaciens* cultured in HEPES-buffered AGW medium with 20 mmol L^{-1} of lactate and synthetic high surface area goethite ($165.1 \text{ m}^2 \text{ g}^{-1}$) as the sole electron acceptor are in good agreement with previous work (42). With an initial cell number of approximately $1.8 \times 10^6 \text{ cells mL}^{-1}$, the total mass of Fe(II) soluble in 0.5 M HCl increased at an initial rate of $0.09 \pm 0.01 \text{ mmol L}^{-1} \text{ h}^{-1}$ (Figure 1) and then asymptotically approached a final concentration of approximately 5.1 mmol L^{-1} . Approximately 50% of the total 0.5 M HCl -soluble Fe(II) was in the aqueous phase, with the remainder being associated with the solid phase. Solution pH (data not shown) increased from pH 7.0 to pH 7.3 over the first 75 h of incubation, slowly increased to a maximum of pH 7.5 at 500 h, and then remained constant for the remainder of the experiment. The final concentration (960 h) of 6 M HCl -soluble Fe(II) was approximately 6 mmol L^{-1} (data not shown). Thus, approximately 12% of the original mass of ferric iron had been reduced, 85% of which can be accounted for by extraction with 0.5 M HCl . The observed rate of 0.5 M HCl -soluble Fe(II) production is considered to be a minimum rate of iron reduction, as a number of Fe(II)-bearing minerals (e.g. magnetite) are not soluble in 0.5 M HCl .

Comparison of Fe(II) data presented in Figure 1 with Zn data presented in Figure 2 reveals a loss of Zn from the weakly bound (soluble in 0.5 M HCl) phase as microbial goethite reduction proceeds. Total Zn remained constant, and the concentration of aqueous Zn did not increase. Therefore, microbial goethite reduction may have immobilized Zn into a new, strongly bound solid phase (soluble in 6 M HCl but not in 0.5 M HCl). Aqueous Zn (data not shown) and total 0.5 M HCl soluble Zn (Figure 6) concentrations remained constant with time in uninoculated controls. To ascertain

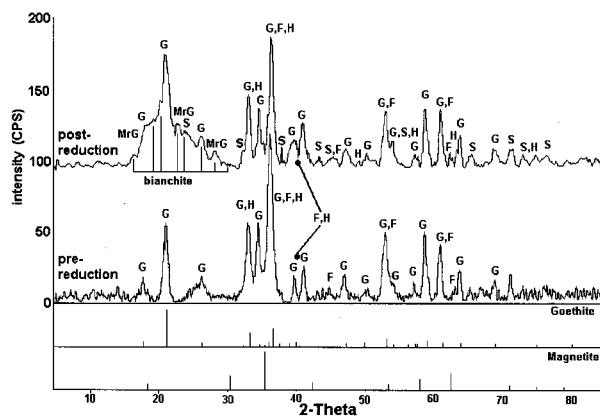


FIGURE 3. X-ray diffractograms for goethite (bottom) and microbially reduced goethite (top). "F" denotes ferrihydrate peaks, "G" denotes goethite peaks, "H" denotes hematite peaks, "S" denotes siderite peaks, and "MrG" denotes peaks for as-yet unidentified minerals that are the result of microbial goethite reduction.

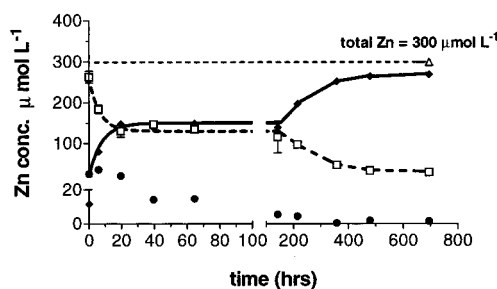


FIGURE 4. Zinc immobilization as a result of microbial lepidocrocite reduction in the absence of NO_3^- . Zn-aqueous (solid circles), Zn-bound (open squares), Zn-strongly bound (solid diamonds), and Zn-total (open triangles) are plotted versus time (h). Trend lines represent the best nonlinear fit to the data.

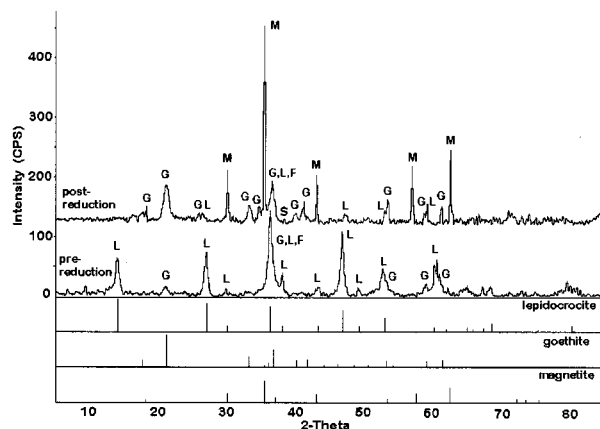


FIGURE 5. X-ray diffractograms for lepidocrocite (bottom) and microbially reduced lepidocrocite (top). "F" denotes ferrihydrate peaks, "G" denotes goethite peaks, "L" denotes lepidocrocite peaks, "S" denotes siderite peaks, and "M" denotes magnetite peaks.

the nature of this new phase, the XRD diffractogram of the original goethite was contrasted with the XRD diffractogram of the microbially reduced goethite (Figure 3). The most notable effects of microbial goethite reduction were the formation of siderite [FeCO_3], a reduction in the height of the peak at $d = 2.5 \text{ nm}$ ($2\Theta = 36$) relative to the other major goethite peaks, and a general broadening of the goethite peak at $d = 4.18 \text{ nm}$ ($2\Theta = 21$). This observed "broadening" of the goethite peak at $d = 4.18 \text{ nm}$ can be attributed to the formation of siderite and poorly crystalline bianchite [$(\text{Zn}, \text{Fe})\text{SO}_4 \cdot 6\text{H}_2\text{O}$]. Based on their d spacing, butlerite [$\text{Fe}(\text{OH})$ -

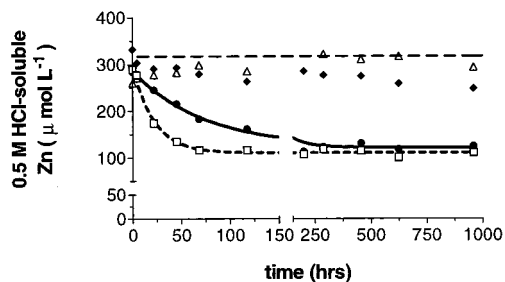


FIGURE 6. Effect of NO_3^- on Zn speciation during microbial goethite reduction. NO_3^- free (open squares), 1 mM NO_3^- (closed circles), 5 mM NO_3^- (closed diamonds), and uninoculated control (open triangles) are plotted versus time (h). Given concentrations represent the bound fraction of Zn. Trend lines represent the best nonlinear fit to the data.

$\text{SO}_4 \cdot 2\text{H}_2\text{O}$], lipscombite $[\text{Fe}(\text{II})\text{Fe}(\text{III})_2(\text{PO}_4)_2(\text{OH})_2]$, phosphosiderite $[\text{FePO}_4 \cdot 2\text{H}_2\text{O}]$, szomolnokite $[\text{FeSO}_4 \cdot \text{H}_2\text{O}]$, ferroxahydrate $[\text{FeSO}_4 \cdot 6\text{H}_2\text{O}]$, and bilinite $[\text{Fe}(\text{II})\text{Fe}(\text{III})_2(\text{SO}_4)_4 \cdot 2\text{H}_2\text{O}]$ could also account for this observed broadening affect. In addition to these major features, minor broadening of the goethite peaks at $d = 2.69$ nm ($2\Theta = 33.2$), $d = 2.25$ nm ($2\Theta = 40$), and $d = 2.19$ nm ($2\Theta = 41$) was observed. This minor broadening may be attributable to the formation of hematite (Fe_2O_3) and siderite, as a number of small peaks that may correspond with these minerals can also be discerned in the postreduction diffractogram. Even though the microbially reduced goethite was a dark, greenish-brown in color, characteristic peaks for green rust (16, 43) were not observed in postreduction XRD diffractograms. Magnetite formation was not observed as a result of microbial goethite reduction.

Results from similar iron reduction experiments with *S. putrefaciens* cultured in HEPES-buffered AGW medium with 20 mmol L^{-1} lactate and synthetic lepidocrocite ($110 \text{ m}^2 \text{ g}^{-1}$) as the sole electron acceptor yielded a slightly different trend. Lepidocrocite reduction still produced 0.5 M HCl-soluble Fe(II) at a high rate (an initial cell mass of approximately 2.0×10^6 cells mL^{-1} produced 0.16 ± 0.04 mmol 0.5 M HCl-soluble Fe(II) $\text{L}^{-1} \text{ h}^{-1}$), with a ratio of aqueous Fe(II) to bound Fe(II) similar to that of goethite (Figure 1). Approximately 200 h after the cessation of 0.5 M HCl-soluble Fe(II) production, both aqueous Fe(II) and total 0.5 M HCl-soluble Fe(II) began to decrease with time while the system was still anaerobic. During this period, the suspended solid developed magnetic properties, and its color changed from brownish orange to black. Solution pH (data not shown) increased from pH 7.1 to pH 7.4 over the first 75 h of incubation, remained at pH 7.4 over the next 125 h, and then slowly decreased back to the initial pH value. The final concentration (695 h) of 6 M HCl-soluble Fe(II) was approximately 10 mmol L^{-1} (data not shown). Thus, approximately 20% of the original mass of ferric iron had been reduced, 18% of which can be accounted for by extraction with 0.5 M HCl.

Comparison of Fe(II) data (Figure 1) with Zn data (Figure 4) suggests that Zn immobilization during reduction of lepidocrocite occurred in two stages. The first stage coincided with active iron reduction, and the second stage coincided with the subsequent period of decreasing 0.5 M HCl-soluble Fe(II). As with goethite, aqueous Zn (data not shown) and total 0.5 M HCl-soluble Zn (Figure 7) concentrations remained constant with time in uninoculated controls. Further comparison of prereduction and postreduction XRD diffractograms for the lepidocrocite experiment (Figure 5) indicates that magnetite is the dominant end product of lepidocrocite reduction under experimental conditions. No lepidocrocite peaks are observed, and, although siderite formation is observed, none of the peak broadening observed in the goethite reduction experiment was seen with the lepi-

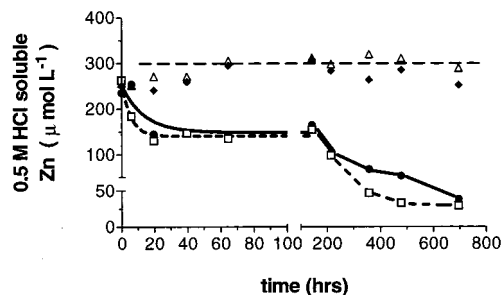


FIGURE 7. Effect of NO_3^- on Zn speciation during microbial lepidocrocite reduction. NO_3^- free (open squares), 1 mM NO_3^- (closed circles), 5 mM NO_3^- (closed diamonds), and uninoculated control (open triangles) are plotted versus time (h). Given concentrations represent the bound fraction of Zn. Trend lines represent the best nonlinear fit to the data.

docrocite. The increase in goethite peak intensity during the course of experimentation is possibly attributable to loss of lepidocrocite relative to the goethite present as a minor contaminant. However, transformation of lepidocrocite to goethite cannot be discounted. Because Zn immobilization via lepidocrocite reduction occurred in two stages, it is possible that the same mineral phase responsible for Zn immobilization in goethite also forms during lepidocrocite reduction. No XRD data are available for the interim period between cessation of Fe reduction and the initiation of 0.5 M HCl-soluble Fe(II) loss, and the subsequent formation of a magnetite surface coating could obscure older mineral phases.

To examine the effect of NO_3^- inhibition of iron reduction on the speciation and mobility of surface-bound Zn, experiments with goethite and lepidocrocite were also performed in bottles amended with NO_3^- . NO_3^- inhibition of Fe(II) production is a well documented phenomenon with both pure cultures of *S. putrefaciens* (28, 29) and enrichment cultures of sediment microbial communities (35, 44). In the goethite reduction experiments (Figure 6), 1 mM NO_3^- (initial concentration) slowed the rate of Zn immobilization but had no effect on the overall extent of this phenomenon. No Zn immobilization is observed in the 5 mM NO_3^- experiment or in the uninoculated control. Fe(II) production follows a similar trend (data not shown). In the lepidocrocite experiments (Figure 7), 1 mM NO_3^- also slowed the rate of Zn immobilization—but to a lesser degree than with goethite. As with goethite, 1 mM NO_3^- had no effect on the overall extent of Zn immobilization, and no Zn immobilization was observed in the 5 mM NO_3^- experiment or in the uninoculated controls.

Discussion

Zinc Immobilization. Our usage of the term Zn immobilization refers to the production of a zinc-containing phase not soluble in a 2-h extraction with cold 0.5 M HCl. Only one period of Zn immobilization was observed during goethite reduction, but Zn immobilization associated with lepidocrocite reduction appeared to follow a two-stage process. The first stage was similar to the results achieved with goethite, but the second stage occurred well afterward when Zn was further immobilized by a process that was accompanied by the loss of 0.5 M HCl-soluble iron. Based on observed changes in oxide color and magnetism (greenish-brown to black, nonmagnetic to magnetic), this second stage of enhanced Zn immobilization was associated with magnetite formation. Transmission electron microscope (TEM) analysis of the magnetite (data not shown) revealed extremely small crystallites (approximately 50 nm) with either hexagonal or acicular lath morphology. Based on the wet chemistry data, the small crystal size, and the fact that Fe(II) and Zn(II)

have the same ionic radius, we surmise that Zn may have been incorporated into the magnetite crystallites.

In all experiments, first-stage immobilization of surface-bound Zn was observed to coincide with microbial production of Fe(II). The rate of Zn immobilization decreased with increasing NO_3^- concentration, and no Zn immobilization was observed when the concentration of NO_3^- was high enough to completely inhibit microbial production of Fe(II). These data, coupled with the observed lack of Zn immobilization in uninoculated control cultures, suggest that Zn immobilization in our system was associated with microbial iron reduction. The observed magnetite-independent immobilization of surface-bound Zn can be explained by either (i) strong complexation of Zn by the binding sites on or in bacterial cells or (ii) incorporation of Zn within a new, 0.5 M HCl-insoluble mineral phase that was formed as a result of microbial production of Fe(II).

Metal uptake by microbial cell walls is a well-known phenomenon. Natural communities of bacteria have been observed to act as sites for metal sorption and mineral precipitation (25), and strong metal uptake has been observed by cell wall and cell envelope isolates of Gram-positive bacteria (19–22, 45, 46), gram negative bacteria (21, 45, 46, 47), and by bacterial biofilms (48). Fein et al. (49) used equilibrium thermodynamics to explain metal interactions with the cell wall of the Gram-positive bacterium, *Bacillus subtilis*, and concluded that metal-surface complexes for Al, Cd, Cu, and Pb were quite stable—but that metal binding was strongly pH-dependent and attributable to carboxyl, phosphate, and hydroxyl sites according to the acid/base properties of the surface. Although *S. putrefaciens* is Gram-negative and may bind much less metal than its Gram-positive counterparts (21), metal-binding to the cell walls is a potential mechanism for reductive immobilization of Zn. However, when Zn was sorbed to cells in preliminary experiments, all Zn was recoverable in 0.5 M HCl extracts (data not shown), suggesting that binding to cell surfaces was not a suitable explanation for the Zn immobilization observed in our experiments.

Mineral nucleation has been observed on microbial cell walls (23–26), and the altered pH and E_h conditions within the microenvironment that exists between an attached bacterial cell and a mineral surface may provide conditions that favor mineral precipitation that would not occur within the bulk chemical environment (7). However, the area of iron oxide surface is more than 100-fold greater than that of the cell surface in these systems—and thus mineral nucleation on the goethite or lepidocrocite surface would be expected to dominate. Because a number of iron minerals are known to not be soluble in dilute HCl (39), biologically induced mineralization can potentially explain the observed degree of Zn immobilization.

Previous work on microbial reduction of hydrous ferric oxide in carbonate-containing media (12) note the importance of siderite as a biologically induced mineral. Even in our low-bicarbonate medium, CO_2 generated by lactate metabolism could produce enough inorganic carbon to precipitate siderite. XRD data indicate the formation of siderite as a result of both microbial goethite reduction (Figure 3) and lepidocrocite reduction (Figure 5). Comparison of the relative heights of the siderite peaks at $d = 2.8 \text{ nm}$ ($2\theta = 31.5$) and $d = 2.35 \text{ nm}$ ($2\theta = 38$) indicates that the siderite generated in this experiment is probably manganoan siderite (ferrous iron substituted with either Mn or Zn). Subsequent analysis of aged, microbially reduced goethite by SEM/EDAX (data not shown) also revealed formation of Zn-enriched siderite. Although the solubility kinetics of Zn-substituted siderite have not been extensively studied, the relatively high solubility of siderite in 0.5 M HCl make it unlikely that siderite formation (in the absence of magnetite production) ac-

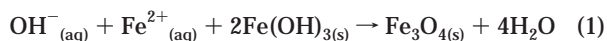
counted for the observed degree of Zn immobilization.

The XRD data may also indicate the formation of various hydrated ferrous/ferric SO_4^{2-} , PO_4^{3-} , and hydroxyl- $\text{SO}_4^{2-}/\text{PO}_4^{3-}$ minerals that may account for the observed degree of Zn immobilization. Very little thermodynamic data are available for these minerals, and thus it is difficult to ascertain if the formation of these minerals is consistent with the slurry composition or if they would be expected to dissolve in 0.5 M HCl. The extremely low PO_4^{3-} concentration ($\sim 44 \mu\text{M}$) seems to exclude the precipitation of significant amounts of hydrated ferrous/ferric phosphate minerals. Beveridge et al. (50) reported the formation of metal phosphate minerals when metal-loaded *B. subtilis* cells are “aged” (sealed, heated to $\sim 100^\circ\text{C}$) in artificial sediment with the cell walls providing the only source of PO_4^{3-} in their system. While it is conceivable that the XRD data reflects the initial stages of amorphous iron phosphate mineral nucleation from cell-wall PO_4^{3-} and surface-bound Fe(II), the low ratio of microbe surface to mineral surface probably precludes this explanation.

A third potential explanation for the observed degree of Zn immobilization involves the enhanced conversion of less-stable iron oxide phases to goethite. Transformation of small amounts of ferrihydrite (present as a minor contaminant) to goethite is supported by the XRD data for goethite reduction (Figure 3), where the height of the main ferrihydrite peak at $d = 2.5 \text{ nm}$ ($2\theta = 36$) relative to the other major goethite peaks was observed to decrease over the course of the experiment. This process may also occur in the lepidocrocite experiment, where the XRD data also indicates that goethite is becoming more prevalent as the experiment progresses. The hypothesis that microbial reduction of iron oxide minerals also enhances the rate of oxide recrystallization and thereby acts to immobilize adsorbed trace metals is consistent with all of our results. However, more advanced spectroscopic data is needed to confirm this hypothesis.

NO_3^- Inhibition of Zn Immobilization. NO_3^- is an agricultural waste product, a byproduct of nuclear fuels processing, and a common groundwater contaminant. Previous research has documented that the presence of NO_3^- can inhibit microbial iron reduction (27, 29, 35), but the impact of competition between NO_3^- reduction and iron reduction on metal geochemistry has been largely overlooked. Our experiments have indicated that the presence of NO_3^- can inhibit Fe(II) production via goethite and lepidocrocite reduction and that this inhibition also blocks the geochemical processes that lead to Zn immobilization within our system.

Magnetite Formation. Extracellular magnetite production has been widely reported to be induced by microbial iron reduction (6–8, 10, 51), but all of these studies have utilized amorphous ferric hydroxide ($\text{Fe}(\text{OH})_3$) as the source of crystalline ferric iron. In this study, we report that magnetite formation can be induced by microbial reduction of lepidocrocite ($\gamma\text{-FeOOH}$). The mechanism of microbial magnetite formation still remains obscure, but the observation that *S. putrefaciens* formed magnetite from lepidocrocite ($\gamma\text{-FeOOH}$) but not from goethite ($\alpha\text{-FeOOH}$) is worthy of further comment. Lovley (8) indicates that magnetite formation is enhanced by high pH and presents the reaction:

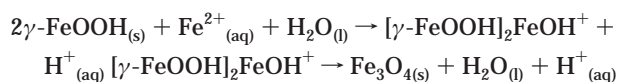


However, no theoretical mechanism is offered. Misawa et al. (52) reported that magnetite formation proceeds via the slow oxidation of ferrous hydroxide and forms either green rusts, green Fe(II)–Fe(III) surface complexes (e.g. $[\text{Fe}(\text{II})_2\text{Fe}(\text{III})\text{-OOH}]^{4+}$), or dark red complexes $[\text{Fe}(\text{II})\text{Fe}(\text{III})_2\text{O}_x(\text{OH})_{2(3-x)}]$ as reaction intermediates. Recent work by Odziemkowski et al. (53) utilized normal and surface-enhanced Raman spectroscopy to identify the reaction intermediates formed during the anaerobic corrosion of metallic iron. Based in

part on the observation that magnetite formation in these systems is preceded by the formation of a surface film of ferrous hydroxide, they proposed a reaction which proceeds via a dissolution/precipitation mechanism and utilizes H^+ as an electron acceptor:



Alternatively, Tamura et al. (54) reported magnetite formation when the pH of a mixture of Fe(II) and lepidocrocite is raised from 5 to 9. Their proposed scheme also involves a ferrous hydroxide intermediate but follows a simpler dissolution/precipitation mechanism and does not involve further oxidation and reduction:



This reaction is initiated above pH 7.3 and requires that the original oxide mineral provide the ferric iron necessary for magnetite formation. Neither Tamura et al. (54) nor Odziemkowski et al. (53) reported the formation of green rusts within their systems, but the proposed reaction intermediates of Tamura et al. (54) and the poorly crystalline ferrous hydroxide surface film observed by Odziemkowski et al. (53) do correlate well with the proposed green complex structures of Misawa et al. (52).

Although there are differences in the redox requirements of these contrasting theories, this earlier work has clearly demonstrated that abiotic magnetite formation proceeds via a ferrous hydroxide intermediate that forms on the ferric oxide surface, and it is likely that microbially induced magnetite formation proceeds via a similar mechanism. Magnetite precipitation must be preceded by the formation of an activated ferrous/ferric hydroxide surface complex, and the ability (or lack thereof) of lepidocrocite and goethite to support magnetite production must be related to their ability to form this reaction intermediate. Bell et al. (7) reports that magnetite formation results from microbial alteration of local E_h and pH conditions. Thus, it is possible that *S. putrefaciens* reduced our preparation of lepidocrocite at a faster rate than goethite, altering local pH and E_h conditions to the point where ferrous hydroxide reaction intermediates are stable and thereby allowing magnetite formation. Our data indicate that the rate of production of 0.5 M HCl-soluble Fe(II) is slightly higher for lepidocrocite (approximately $0.16 \text{ mmol L}^{-1} \text{ h}^{-1}$) than for goethite (approximately $0.09 \text{ mmol L}^{-1} \text{ h}^{-1}$). In addition, the lepidocrocite slurries produced approximately 10 mmol L^{-1} of 6 M HCl-soluble Fe(II) by the end of the experiment as opposed to approximately 6 mmol L^{-1} of 6 M HCl-soluble Fe(II) for the goethite experiment. Trace amounts of ferrihydrite in our oxide preparation may also have affected apparent oxide reduction rates. While these data indicate a faster reduction rate for our preparation of lepidocrocite, other data contradict this mechanism of promoting magnetite formation. In both systems, bulk pH rose above the critical point of 7.3 that Tamura et al. (54) indicated was necessary for magnetite formation, and XRD data indicate that goethite is preserved in the lepidocrocite culture.

Steric hindrance in the formation of inner sphere Fe(II)Fe(III)-hydroxide complexes may also prevent magnetite formation in microbe-goethite systems, as there are significant structural differences between the goethite and lepidocrocite polymorphs. Both goethite and lepidocrocite consists of double bands of edge-sharing $FeO_3(OH)_3$ octahedra. In goethite, the double bands are linked by corner sharing in a fashion that forms extremely small 2×1 octahedra "tunnels" that are crossed by hydrogen bridges

(38). In lepidocrocite, the double bands of octahedra share edges to form zigzag layers that are connected by hydrogen bonds (38).

If microbially induced magnetite formation follows the mechanism presented by Tamura et al. (54), then magnetite formation may occur in lepidocrocite because the layered, zigzag structure is open enough to allow the formation of inner sphere complexes between large ferrous hydroxide ligands and multiple Fe(III) ions located within the crystal structure. This type of surface complexation may not be possible with the closed structure of goethite. The observation that lepidocrocite reduction produces magnetite while goethite reduction does not would not be expected in a ferrous hydroxide oxidation mechanism (53), where inner-sphere surface complexes between crystalline ferric iron and surface ferrous hydroxide are not necessary for magnetite formation. Nevertheless, molecular-level data that can discern ferrous hydroxide surface coatings from surface complexes between ferrous hydroxide and crystalline ferric iron are necessary before the true nature of this mechanism can be determined.

Acknowledgments

We gratefully acknowledge the Department of Energy program in Natural and Accelerated Bioremediation (DOE Grant no. DE-FG02-97ER62482) for funding this research. We also thank Dr. Matilde Urrutia for performing the surface area analyses, Dr. Yuri Gorby for providing SEM/EDAX data, and Dr. Eric Roden, Dr. John Zachara, and Dr. Rona Donahoe for helpful discussions.

Literature Cited

- (1) Lovley, D. R.; Phillips, E. J. P. *Appl. Environ. Microbiol.* **1988**, *54*, 1472–1480.
- (2) Lovley, D. R. *Geomicrobiol. J.* **1987**, *5*, 375–398.
- (3) Lovley, D. R. *Microbiol. Rev.* **1991**, *55*, 259–287.
- (4) Myers, C. R.; Nealson, K. H. *Iron mineralization by bacteria: metabolic coupling of iron reduction to cell metabolism in Alteromonas Putrefaciens strain MR-1*; Myers, C. R., Nealson, K. H., Ed.; Plenum Press: New York, 1990; pp 131–149.
- (5) Lovley, D. R.; Phillips, E. J. P. *Appl. Environ. Microbiol.* **1986**, *51*, 683–689.
- (6) Konhauser, K. O. *Earth-Science Rev.* **1998**, *43*, 91–121.
- (7) Bell, P. E.; Mills, A. L.; Herman, J. S. *Appl. Environ. Microbiol.* **1987**, *53*, 2610–2616.
- (8) Lovley, D. R. *Magnetite formation during microbial dissimilatory iron reduction*; Lovley, D. R., Ed.; Plenum Press: New York, 1990; pp 151–166.
- (9) Lovley, D. R.; Stolz, J. F.; Nord, G. L.; Phillips, E. J. *Nature* **1987**, *330*, 252–254.
- (10) Moskowitz, B. M.; Frankel, R. B.; Lovley, D. R. *Geophys. Res. Lett.* **1989**, *16*, 665–668.
- (11) Zhang, C.; Liu, S.; Phelps, T. J.; Cole, D. R.; Horita, J.; Fortier, S. M.; Elles, M.; Valley, J. W. *Geochim. Cosmochim. Acta* **1997**, *61*, 4621–4632.
- (12) Frederickson, J. K.; Zachara, J. M.; Kennedy, D. W.; Dong, H.; Onstott, T. C.; Hinman, N. W.; Li, S. *Geochim. Cosmochim. Acta* **1998**, *62*.
- (13) Hansen, H. C. B.; Koch, C. B.; Nancke-Krogh, H.; Borggaard, O. K.; Sørensen, J. *Environ. Sci. Technol.* **1996**, *30*, 2053–2056.
- (14) Ottley, C. J.; Davison, W.; Edmunds, W. M. *Geochim. Cosmochim. Acta* **1997**, *61*, 1819–1828.
- (15) Sørensen, J.; Thorling, L. *Geochim. Cosmochim. Acta* **1991**, *55*, 1289–1294.
- (16) Hansen, H. C. B.; Borggaard, O. K.; Sørensen, J. *Geochim. Cosmochim. Acta* **1994**, *58*, 2599–2608.
- (17) Tessier, A.; Rapin, F.; Carnigan, R. *Geochim. Cosmochim. Acta* **1985**, *49*, 183194.
- (18) Cummings, D. E.; Caccavo, F.; Fendorf, S.; Rosenzweig, R. F. *Environ. Sci. Technol.* **1999**, *33*, 723–729.
- (19) Beveridge, T. J.; Murray, R. G. E. *J. Bacteriol.* **1976**, *127*, 1502–1518.
- (20) Beveridge, T. J.; Forsberg, C. W.; Doyle, R. J. *J. Bacteriol.* **1982**, *150*, 1438–1448.
- (21) Beveridge, T. J.; Fyfe, W. S. *Can. J. Earth Sci.* **1985**, *22*, 1893–1898.

- (22) Doyle, R. J.; Matthews, T. H.; Streips, U. N. *J. Bacteriol.* **1980**, *143*, 471–480.
- (23) Schultze-Lam, S.; Harauz, G.; Beveridge, T. J. *J. Bacteriol.* **1992**, *174*, 7971–7981.
- (24) Southam, G.; Beveridge, T. J. *Appl. Environ. Microbiol.* **1992**, *58*, 1904–1912.
- (25) Konhauser, K. O.; Fyfe, W. S.; Ferris, F. G.; Beveridge, T. J. *Geology* **1993**, *21*, 1103–1106.
- (26) Konhauser, K. O. *FEMS Microbiol. Rev.* **1997**, *20*, 315–326.
- (27) Obuekwe, C. O.; Westlake, D. W. S.; Cook, F. D. *Can. J. Microbiol.* **1981**, *27*, 692–697.
- (28) Obuekwe, C. O.; Westlake, D. W. S. *Microbiol. Lett.* **1982**, *19*, 57–62.
- (29) DiChristina, T. J. *J. Bacteriol.* **1992**, *174*, 1891–1896.
- (30) Nealson, K. H.; Saffarini, D. *Annu. Rev. Microbiol.* **1994**, *48*, 311–343.
- (31) Picardal, F. W.; Arnold, R. G.; Couch, H.; Little, A. M.; Smith, M. E. *Appl. Environ. Microbiol.* **1993**, *59*, 3763–3770.
- (32) Kim, S.; Picardal, F. W. *Environ. Tox. Chem.* **1999**, *18*, 2142–2150.
- (33) Riley, R. G.; Zachara, J. M. *Identification of the Most Common Contaminant Classes*; Riley, R. G., Zachara, J. M., Eds.; U.S. Department of Energy: Washington, DC, 1992; Vol. DOE/ER-0547T, pp 15–17.
- (34) Kooner, Z. S. *Environ. Geol.* **1993**, *21*, 242–250.
- (35) Achtnich, C. A.; Bak, F.; Conrad, R. *Biol. Fertil. Soils* **1995**, *19*, 65–72.
- (36) Semple, K. M.; Westlake, D. W. S. *Can. J. Microbiol.* **1987**, *33*, 366–371.
- (37) Obuekwe, C. O. *Microbial corrosion of crude oil pipeline*; Ph.D.; University of Alberta: Edmonton, 1980.
- (38) Schwertmann, U.; Cornell, R. M. *Iron oxides in the Laboratory*; VCH Publishers Inc.: New York, 1991.
- (39) Kostka, J. E.; Luther, G. W. *Geochim. Cosmochim. Acta* **1994**, *58*, 1701–1710.
- (40) Roden, E. E.; Zachara, J. M. *Environ. Sci. Technol.* **1996**, *30*, 1618–1628.
- (41) Stookey, L. L. *Anal. Chem.* **1970**, *42*, 779–781.
- (42) Roden, E. E.; Zachara, J. M. *Environ. Sci. Technol.* **1996**, *50*, 1618–1628.
- (43) Génin, J. R.; Bourrié, G.; Trolard, F.; Abdelmoula, M.; Jaffrezic, A.; Refaite, P.; Maitre, V.; Humbert, B.; Herbillon, A. *Environ. Sci. Technol.* **1998**, *32*, 1058–1068.
- (44) Sørensen, J. *Appl. Environ. Microbiol.* **1982**, *43*, 319–324.
- (45) Mullen, M. D.; Wolf, D. C.; Ferris, F. G.; Beveridge, T. J.; Flemming, C. A.; Bailey, G. W. *Appl. Environ. Microbiol.* **1989**, *55*, 3143–3149.
- (46) Flemming, C. A.; Ferris, F. G.; Beveridge, T. J.; Bailey, G. W. *Appl. Environ. Microbiol.* **1990**, *56*, 3191–3203.
- (47) Beveridge, T. J.; Koval, S. F. *Appl. Environ. Microbiol.* **1981**, *42*, 325–335.
- (48) Ferris, F. G.; Schultze, S.; Witten, T. C.; Fyfe, W. S.; Beveridge, T. J. *Appl. Environ. Microbiol.* **1989**, *55*, 1249–1257.
- (49) Fein, J. B.; Daughney, C. J.; Yee, N.; Davis, T. A. *Geochim. Cosmochim. Acta* **1997**, *61*, 3319–3328.
- (50) Beveridge, T. J.; Meloche, J. D.; Fyfe, W. S.; Murray, R. G. E. *Appl. Environ. Microbiol.* **1983**, *45*, 1094–1108.
- (51) Lovley, D. R.; Stoltz, J. F.; Nord, G. L.; Phillips, E. J. P. *Nature* **1987**, *330*, 252–254.
- (52) Misawa, T.; Hashimoto, K.; Shimodaira, S. *Corr. Sci.* **1974**, *14*, 131–149.
- (53) Odziemkowski, M. S.; Schuhmacher, T. T.; Gillham, R. W.; Reardon, E. J. *Corr. Sci.* **1998**, *40*, 371–389.
- (54) Tamaura, Y.; Ito, K.; Katsura, T. *J. Chem. Soc., Dalton Trans.* **1983**, 189–194.

Received for review May 3, 1999. Revised manuscript received October 5, 1999. Accepted October 14, 1999.

ES990510X